ALGORITHMS FOR SEAWIFS STANDARD PRODUCTS DEVELOPED WITH THE CALCOFI BIO-OPTICAL DATA SET

B. GREG MITCHELL AND MATI KAHRU
Scripps Institution of Oceanography
University of California, San Diego
9500 Gilman Drive
La Jolla, California 92093-0218
gmitchell@ucsd.edu
mkahru@ucsd.edu

ABSTRACT

Funding from NASA's Ocean Biogeochemistry Program and the Goddard Space Flight Center SeaWiFS Project was used to implement an ocean optics program as part of the routine cruises of the California Cooperative Oceanic Fisheries Investigations (CalCOFI). Since August 1993, data from more than 300 bio-optical stations have been acquired, merged with complementary data, and made available for developing remote sensing algorithms. The profiling instrument consisted of a Biospherical Instruments, Inc. MER-2040/2041 radiometer integrated with CTD probes, a transmissometer, and a fluorometer. A detailed calibration time series of the radiance and irradiance sensors has been maintained to ensure maximum accuracy. The data set has been used to develop empirical algorithms for SeaWiFS standard products including chlorophyll a (chl a), "CZCS pigments," and diffuse attenuation coefficient $K_d(490)$. Algorithms using cubic regressions of remote sensing reflectance (R_{rs}) ratios provided the best estimation of chl a and pigments over the full range of chl a (0.05–22.3 mg m^{-3}). Multiple linear regressions of multiple-band ratios proved to be less robust. Relationships between spectral K and chl a suggest that previous K algorithms may have errors due to estimates of pure-water absorption.

INTRODUCTION

The Southern California Bight region, from San Diego to just north of Point Conception, is a region with one of the longest, most comprehensive time series of marine observations—California Cooperative Oceanic Fisheries Investigations (CalCOFI)—which has been jointly sponsored by the National Oceanic and Atmospheric Administration (NOAA), the University of California, and the California Department of Fish and Game for more than 40 years. The Southern California Bight is part of the California Current system, a region which has been well studied with respect to its regional optical properties in an effort to develop regional ocean color algorithms (Smith and Baker 1978a, b; Gordon et al. 1983; Mitchell and Kiefer 1988; Sosik and Mitchell 1995).

The CalCOFI region encompasses a large dynamic range of coastal and open-ocean trophic structure. Optics data have been collected for chl a concentrations at the surface ranging over three orders of magnitude, from 0.05 mg m^{-3} for offshore stations to over 50 mg m^{-3} during a massive red tide bloom at Scripps Pier. The taxonomic composition across the onshore-offshore gradient ranges from a dinoflagellate/diatom-dominated coastal community to a picoplankton-dominated community offshore. The offshore region of CalCOFI is typical of the open-ocean oligotrophic subtropical gyres, with low surface chl a, a deep chl a maximum between 100 and 130 m, and a nutricline between 120 and 150 m.

The current CalCOFI station grid (fig. 1) has 66 stations. On each cruise, approximately 25 of the CalCOFI stations are suitable for remote sensing reflectance measurements during daylight hours.

METHODS

Instruments

An integrated underwater profiling system was used to collect optical data and to characterize the water column. The system includes an underwater MER-2040 radiometer (Biospherical Instruments, Inc., S/N 8738) that measures depth, downwelling spectral irradiance (E_d), and upwelling radiance (L_u) at the following nominal wavelengths: 340, 380, 395, 412, 443, 455, 490, 510, 532, 555, 570, and 665 nm. The E_d block also included PAR (phytosynthetically available radiation); the

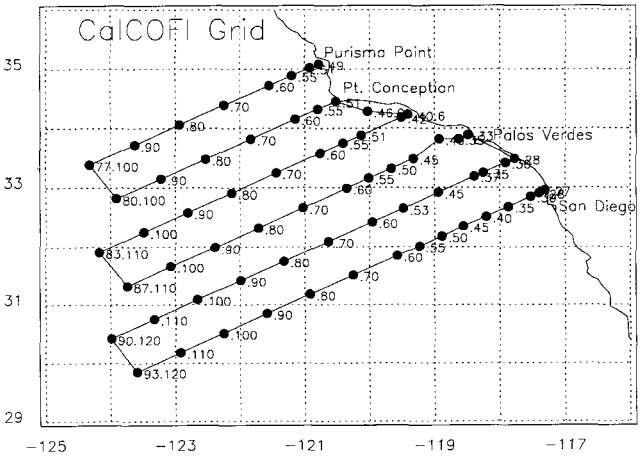

Figure 1. The CalCOFI station grid.

[Manuscript received November 10, 1997.]

L_u block included natural fluorescence. A MER-2041 deck-mounted reference radiometer (Biospherical Instruments, Inc., S/N 8739) measured downwelling irradiance at the following nominal wavelengths: 340, 380, 395, 412, 443, 490, 510, 555, 570, 665, 780, and 875 nm, PAR. The MER-2040 was also interfaced to a 25 cm transmissometer (SeaTech Inc.), a fluorometer (Wetlabs Inc.), and conductivity and temperature probes (Sea-Bird Electronics Inc.).

The underwater instrumentation was integrated onto a stainless steel frame. Power was provided to all systems via the MER-2040. Data from all instruments were multiplexed through the MER-2040 for transmission to the surface through submarine 3-conductor cable on an oceanographic winch equipped with a slip ring.

Instrument Characterization and Radiometric Calibrations

The MER-2040/2041 system used in this study has had detailed system characterization and radiometric calibration performed by the manufacturer, Biospherical Instruments, Inc. (BSI), and the Center for Hydro-Optics and Remote Sensing (CHORS) of San Diego State University according to procedures specified by the SeaWiFS Protocols (Mueller and Austin 1995). The unit was characterized by CHORS for spectral bandpass and for the immersion coefficient and cosine response of the cosine collector (Mueller 1995). A calibration and spectral band characterization was also obtained from the University of California, Santa Barbara, Institute for Computational Earth System Science (UCSB ICESS). The instrument specifications called for band centers within 1 nm of the nominal BSI band center. The reported spectral band centers measured by CHORS differ by more than 1 nm from the BSI nominal band centers for 5 out of 12 channels; two of those are SeaWiFS bands. The UCSB calibration found all SeaWiFS bands to be within 1 nm of the BSI nominal band center. The maximum difference found by UCSB is 3.1 nm for the "380" nm channel (table 1). All data are reported in terms of the "BSI nominal" band centers. Experimental determinations by BSI and CHORS were in good agreement for cosine response and immersion coefficient for the cosine collector.

Radiometric calibrations of the instrument were performed relative to National Institute of Standards and Technology (NIST) standard FEL lamps. During the period corresponding to this data set, BSI performed 10 calibrations and CHORS performed 3. The unit was calibrated at BSI, CHORS, and UCSB between May and November 1995. The differences in calibration between BSI and UCSB were within about 1% for E_d and within 2% for L_u; slightly higher differences were observed between BSI and CHORS (figs. 2 and 3). Some of the differences in the UV bands may be attributable to the differences in the spectral bandpass characteriza-

TABLE 1
Measured E_d Band Centers as Determined by UCSB and CHORS, Compared with the Nominal BSI Centers for MER-2040-8738

BSI nominal wavelength, nm	UCSB center—BSI nominal, nm	CHORS center—BSI center, nm
340	−1.7	−1.4
380	−3.1	−2.4
395	0.9	1.6
412	−0.6	0.0
443	0.2	0.8
455	−0.7	0.1
490	0.3	1.1
510	−1.0	−0.1
532	−0.3	0.0
555	0.3	0.0
570	−0.6	0.0
665	0.4	1.5

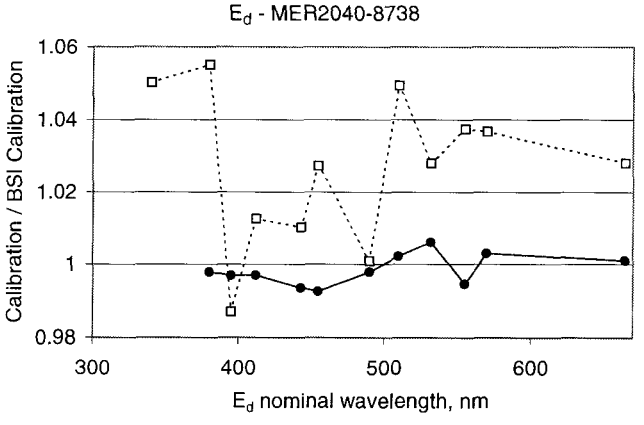

Figure 2. A comparison of MER-2040 E_d calibrations by different laboratories: ratio of UCSB calibration on 18 May 1995 to BSI calibration on 2 June 1995 (filled circles), and ratio of CHORS calibration on 2 Nov. 1995 to BSI calibration on 25 Nov. 1995 (open squares).

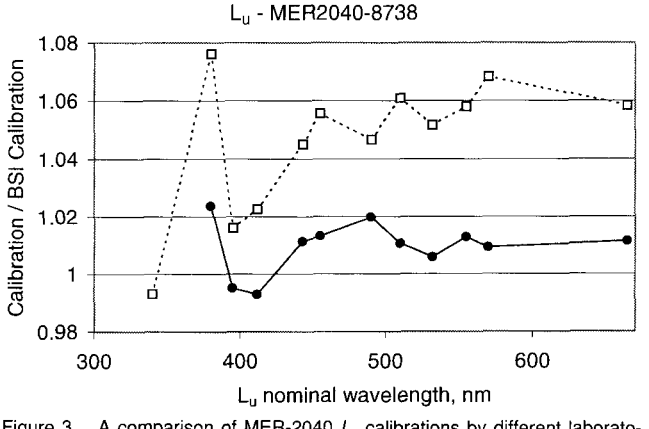

Figure 3. A comparison of MER-2040 L_u calibrations by different laboratories: ratios of UCSB calibration on 18 May 1995 to BSI calibration on 2 June 1995 (filled circles), CHORS calibration on 2 Nov. 1995 to BSI calibration on 25 Nov. 1995 (open squares).

tion (table 1). Also, lamp energy in the UV is low, causing greater calibration error. Our participation in the NASA SeaWiFS Project SIRREX activities and the multiple calibrations of MER 8738/8739 at different laboratories leads to the conclusion that the overall interlab calibrations approach the minimum requirement set by the SeaWiFS protocols (Mueller and Austin 1995), which call for calibration reproducibility of better than 5%. However, the goal of absolute calibration within ±1% has not been attained. Details of the in-water instrument calibration efforts can be found in Mueller at al. (1994).

Reasonable agreement between BSI calibrations and those of independent laboratories and the fact that more calibrations were from BSI justified using the BSI calibrations exclusively for determining the calibration time series for processing CalCOFI data.

The experimental immersion coefficients for E_d were provided by CHORS (Mueller 1995). The immersion coefficients for the L_u window were based on the window material refractive index and were changed after cruise CAL9308, when the original window composed of Schott glass UBK7 cracked because of mishandling and was replaced with a quartz glass window, which has been used on all subsequent cruises.

The radiometric calibration coefficients for each channel of each cruise were found as linear interpolations to the middle date of each cruise by using all calibrations performed at BSI since the instrument was manufactured. Even for channels that are stable over time, this procedure of interpolating the time series is a superior approach to using the most recent calibration, since each calibration has analytical error of several percent, and some of this is compensated by taking a longer-term statistical fit to the data. For channels with significant trends, a time-series fit of the data is essential.

An example of the scatter of individual calibration results and the resulting linear interpolation used in the processing of the MER data is shown in figure 4. The 95% confidence limits and the trend regression in figure 4 illustrate that individual calibration points can deviate outside the significance bounds of the trend. These are probably caused by NIST standard lamp transfers, calibration lamp degradation, and technical aspects of executing each calibration (Mueller et al. 1994). Several channels show significant trends, most notably the L_u (555 nm) channel example shown in figure 4, but also the 340 nm channel. Because the E_d (340 nm) channel filter/detector assembly was replaced in June 1995, a dual linear interpolation was used for this channel.

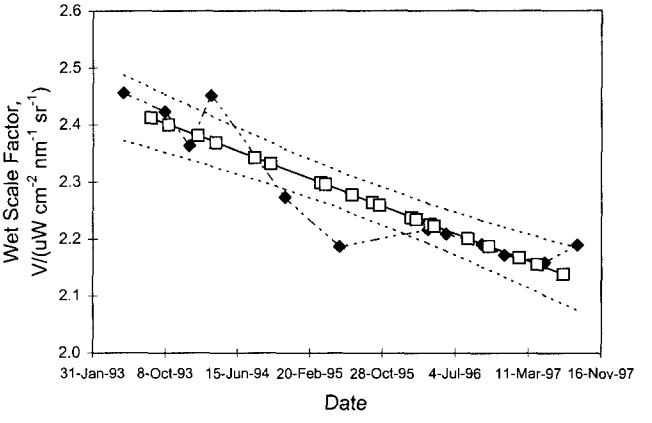

Figure 4. Calibration time series of the MER-2040 L_u (555 nm). Filled symbols are the actual calibrations performed at BSI. The straight line with open symbols is the interpolated wet-scale factor plotted against the middle date of a CalCOFI cruise. Dashed lines are ±95% confidence limits. Similar interpolations are used for all the E_d and L_u channels.

Profiling Procedure

The MER-2040 unit and associated underwater instruments were deployed from the ship's stern A-frame on each station, in accordance with SeaWiFS bio-optical protocols (Mueller and Austin 1995). When skies were clear, partly cloudy, or thinly overcast, the ship was typically oriented with its stern toward the sun to minimize the ship's shadow. This was not always possible because of winds or sea state, so some casts have significant contamination from ship shadow.

The instrumentation was held near the surface for 5–10 minutes before starting the downcast to allow for temperature equilibration and to prime the pump for the Sea-Bird conductivity and temperature system. Winch speed during the cast was kept between 20 and 30 m per minute for most profiles, and the nominal sampling speed of the MER was approximately 2–4 Hz. This achieved a typical sampling density of more than four samples per meter. The MER unit was generally deployed immediately before or immediately after the CalCOFI water bottle cast to ensure minimal offset in time/space for the optics and the pigment data set.

Immediately following each cast, a dark scan of the MER radiometer was run by attaching opaque PVC caps on the radiometer heads and recording the data for several minutes. Dark scan records were evaluated, and the median dark scan for each channel provided the basis for setting lower radiometric thresholds (ten times the dark voltage) for data processing (see below). Dark scans done at the end of profiles differ from dark scans done at BSI during routine calibrations by less than 5% for most channels, but by 10%–20% for several channels. Such differences are negligible for the near-surface data presented here because our exclusion threshold is ten times the median dark voltage for a cruise.

Processing of MER Vertical Profiles

The CalCOFI bio-optical profiles were processed with a modified version of the Bermuda Bio-Optics Project

(BBOP) data-processing system (Siegel et al. 1995). The BBOP system was found most suitable because of its modularity and the ease of adding new filters. The BBOP filters operate on the so-called LCD file format, which is a self-contained ASCII file with the pertinent header, calibration, and processing history included. The implementation of the BBOP processing scheme was adapted and modified in order to increase processing speed, reduce disk access, remove unnecessary complexity, and add new filters. The large set of UNIX shell scripts was completely replaced with a single Perl script, and the proliferating "list" files were replaced with two control files. Modifications were done to the suite of C and C++ programs with the purpose of streamlining the whole process. Added filters include adjustment of the depth of the different variables according to the position of the particular sensor in relation to the depth sensor, and thresholding low radiance or irradiance values in relation to the dark values. Some filters were made more versatile; for example, the binning filter can now produce vertical bins in any float interval starting from 10 cm instead of integer meters. Vertical bins smaller than 1 m were essential for processing profiles with very high attenuation or for very shallow water.

The new processing scheme resulted in almost ten times faster execution speed compared to the original implementation. The speed increase was mostly due to reduced disk access. Because of the increased speed it was found more convenient to do a full reprocessing starting with the raw data whenever a new calibration was implemented, rather than to modify the existing LCD files. All source files of the modified BBOP code as well as the executables for IRIX 5.3 are available for downloading from *ftp://spg.ucsd.edu/pub/bbop*.

In order to ensure compatible depth values with the Marine Life Research Group's rosette-CTD system, we calibrated the MER depth sensor by using linear regression on the depths of a large number of distinct features (e.g., fluorescence maximum, transmission minimum, or bottom of the mixed layer) in profiles measured with both systems.

A typical sequence of operations performed with a set of data files collected with the MER-2040/2041 system consisted of three steps: preprocessing, BBOP processing, and postprocessing.

Preprocessing. Preliminary processing either during a cruise or immediately after the cruise creates hard-copy plots of the vertical profiles. The at-sea procedure is run on a PC under DOS/Windows and includes transforming the MER binary file into a preliminary LCD file, breaking the LCD file into separate downcast and upcast files, and making hard-copy plots of the selected variables. The plots are used for visual quality inspection of the profiles, selecting the depth intervals for the surface extrapolation, and defining the depth of the surface mixed layer. Each profile is given a quality ranking.

Control files listing the MER files to be processed, the filters to be run, and the parameters needed are created either by exporting the necessary fields from a database, or manually with an editor. The auxiliary information includes the corresponding calibration and dark files, dates, coordinates, vertical binning interval, depth range for surface extrapolation, mixed-layer depth range, interval for calculating K, and a quality flag. Calibration files are created for each cruise and MER instrument, and are based on the middle date of the cruise and the calibration history (see earlier section Instrument Characterization and Radiometric Calibrations). The calibration files are updated when new calibration data become available. Time series of the dark scans are created for each cruise. The median dark voltages for each channel for each cruise are used to flag data smaller than ten times the corresponding dark voltage.

BBOP processing. The sequence of the different filters applied to the MER vertical profiles is given in table 2.

Postprocessing and quality control. The MER data from depths corresponding to water samples and the surface extrapolation (0^-) are imported into a relational database (in Microsoft Access). In the database the MER data are linked to results from discrete water samples (e.g., absorption spectra of particulate, detrital, and soluble material) and the hydrographic data from the CalCOFI IEH files.

When measured by an instrument of a finite size, $L_u(\lambda)$ is affected by the instrument's own shadow (Gordon and Ding 1992). The self-shading correction scheme recommended by Mueller and Austin (1995) has been implemented in the analysis since 1997 (see Kahru and

TABLE 2
Summary of the BBOP Processing of Bio-Optical Vertical Profiles

Number	Filter	Description
1	mer2lcdn	Reads binary data file and creates LCD file.
2	insertcastid	Inserts cruise and cast information.
3	mkbin	Bins the data to a regularly spaced vertical grid (typically 1.0 m), partitions the file into down- and upcasts.
4	mkfutil	Deletes unnecessary variables.
5	mkh2o	Calculates salinity and sigma-t.
6	mkshift	Shifts the E_d samples up the number of bins closest to 75 cm.
7	bbopdeflag	Deletes bins with no samples.
8	thresh	Flags values below threshold.
9	mkscalc	Extrapolates some variables to the surface (0^- depth).
10	mkkc	Calculates the diffuse attenuation coefficients K for E_d.
11	ksurf	Extracts the surface diffuse attenuation coefficient K from results of mkscalc and inserts into the surface (0^-) record.

Mitchell, in press, for details). In the analysis reported here the self-shading was ignored. The median error resulting in underestimating L_u for the SeaWiFS bands (excluding 665 nm) of the CalCOFI data was 1%–2%; the maximum error was about 20% for high-pigment water.

For calculating the remote sensing reflectance just above the sea surface $R_{rs}(0^+,\lambda)$, we used the equation

$$R_{rs}(0^+,\lambda) = 0.54\, L_u(0^-,\lambda)/[1.04\, E_d(0^-,\lambda)] \quad (1)$$

Here $L_u(0^-,\lambda)$ is the upwelling radiance extrapolated to just below the sea surface; $E_d(0^-,\lambda)$ is the downwelling irradiance extrapolated to just below the sea surface; and the coefficients 0.54 and 1.04 are the transfer coefficients of the air-sea interface for, respectively, L_u and E_d (Austin 1974). Calculation of $R_{rs}(0^+,\lambda)$ from the surface irradiance measured by the MER-2041 deck unit $E_s(\lambda)$ was also evaluated:

$$R_{rs}(0^+,\lambda) = 0.54\, L_u(0^-,\lambda)/E_s(\lambda) \quad (2)$$

Although both equations 1 and 2 gave similar results, the variability of equation 2 was higher, and the number of stations where equation 2 could be applied was smaller (because of missing MER-2041 data on some cruises). The greater variance when equation 2 was applied is attributed to surface phenomena such as ship shadowing and wave focusing, which affect both E_d and L_u on the MER-2040, but not E_s on the MER-2041. Time/space offsets when shadows from clouds or the ship's superstructure affect the above-water and in-water sensors differently can also contribute to errors in equation 2. Therefore, we used equation 1 for the analysis reported here.

We estimated the surface-layer diffuse attenuation coefficients $K_d(\lambda)$ from the depth range that was used to derive the $L_u(0^-,\lambda)$ and $E_d(0^-,\lambda)$ surface extrapolations. For comparison to previous $K_d(490)$ algorithms and the relationship between $K_d(\lambda)$ and $K_d(490)$, we transformed the remote sensing reflectance to the normalized water-leaving radiance as $L_{WN}(\lambda) = R_{rs}(0^+,\lambda)^* F_0(\lambda)$, where $F_0(\lambda)$ is the mean extraterrestrial irradiance.

The entire MER data set of $E_d(z,\lambda)$, $L_u(z,\lambda)$, $E_s(\lambda)$ is reprocessed as updated calibration files become available or modifications are found necessary. Current data sets are available from NASA's SeaWiFS project SeaBASS archive *(http://seabass.gsfc.nasa.gov)*.

Water Sampling

The general hydrographic data, including the fluorometric pigment concentrations for the CalCOFI cruises, were collected by the Marine Life Research Group of the Scripps Institution of Oceanography (SIO) and were obtained from the CalCOFI data archives *(http://nemo.ucsd.edu)*. Water sampling during CalCOFI cruises was done with a CTD-rosette system separate from the MER profiler. The time delay between those two casts was sometimes more than 1 hr. The resulting errors introduced into the matching of MER data to the water samples due to the spatiotemporal variability may be significant, especially for coastal stations.

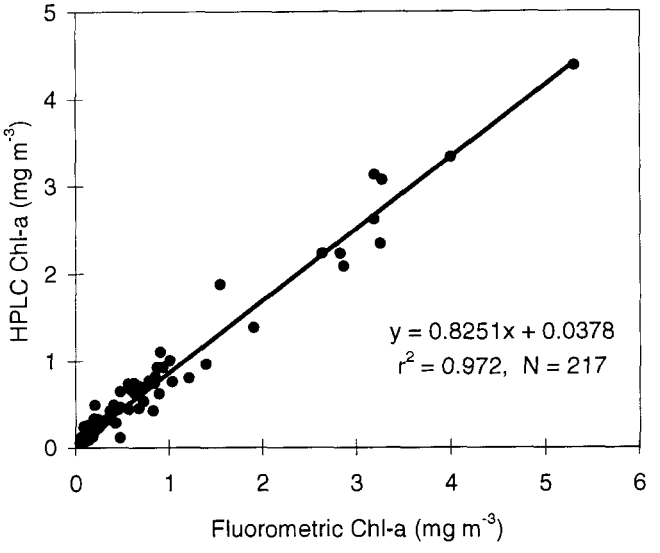

Figure 5. Correlation between fluorometric estimate of chl a and the HPLC estimate. The HPLC estimate is based on the sum of chlorophyll a, chlorophyllide a, allomerized chlorophyll a, divinyl chlorophyll a, and chlorophyll a'. Data presented here are for the upper mixed layer only.

Pigments

The chl a and phaeopigment concentrations used here were determined with the fluorometric method (Holm-Hansen et al. 1965; Venrick and Hayward 1984). High-performance liquid chromatography (HPLC) measurements of chl a with the method of Goericke and Repeta (1993) showed a consistent relationship with the fluorometric results for surface chl a in the range 0.05–5 mg/m^3 (fig. 5). However, the HPLC chl a estimate is about 82% of the fluorometric chl a estimate. This difference is in agreement with the findings of Bricaud et al. (1995). HPLC estimates for chl a are available for approximately half of the optics stations, so we used the fluorometric data for algorithm development.

Statistical Methods

Depending on the variance of a data set, either the reduced major axis (RMA) type II linear regression model (Ricker 1973; Laws and Archie 1981) or the "robust" least absolute deviation linear regression (Press et al. 1990) was used to compute the linear slope and intercept between variables. The "robust" method is preferable in the case of outliers because of various measurement errors. Outliers were usually determined as the points outside two standard deviations of the initial "robust" regression. The remaining points were then run through

either the RMA or the "robust" linear regression models. The root mean square (RMS) error formula used was the same as that of O'Reilly et al. (in press).

RESULTS

The CalCOFI Data Set

A total of thirteen CalCOFI cruises made from 1993 to 1996 are summarized in table 3. More than 300 coincident MER profiles and surface pigment measurements were made. Data from a massive red tide event in the spring of 1995 is reported elsewhere (Kahru and Mitchell, in press).

The frequency distribution of chl a in the CalCOFI data set (fig. 6) deviates from an ideal lognormal distribution that has been proposed before (e.g., Campbell and O'Reilly 1988) and may be better approximated by a sum of two or more lognormal distributions corresponding to the different regimes (oligotrophic, coastal).

Surface Irradiance vs. In-Water Irradiance

The relationship between $E_d(0^-,\lambda)$ determined by extrapolation of the MER-2040 underwater profile to just below the surface, and $E_s(\lambda)$ measured by the MER deck unit is shown in figure 7. The relationships at 412–555 nm have a curvature (demonstrated by the slightly better fits of the power function compared to the linear regression). This may be due to the effect of decreasing transmittance of the air-water interface at large solar zenith angle.

Except for 665 nm, the surface loss of E_d (z, λ) through the air-sea interface as estimated by the slope of the linear fit is higher than the often quoted 4% value (Austin 1974). Our data have been collected in diverse conditions including early morning, late evening, cloudy skies, and rough seas. All of these factors may contribute to the elevated air-sea loss compared to the 4% for ideal conditions.

The slope coefficients range from 1.07 (at 555 nm) to 1.10 (at 412 and 443 nm). As expected, E_d (0^-, 665 nm) data are more noisy as a result of surface extrapolation errors (due to strong attenuation of light at this wavelength) and possible chl a fluorescence. The slope of less than 1.0 may be partially due to natural fluorescence source terms in the underwater data.

TABLE 3
Summary of the CalCOFI Bio-Optical Data Set

Cruise	Starting date	Ending date	Number of MER stations
CAL9308	11 Aug. 93	26 Aug. 93	28
CAL9310	11 Oct. 93	25 Oct. 93	17
CAL9401	17 Jan. 94	8 Feb. 94	30
CAL9403	22 Mar. 94	7 Apr. 94	32
CAL9408	5 Aug. 94	21 Aug. 94	21
CAL9410	30 Sept. 94	16 Oct. 94	25
CAL9504	6 Apr. 95	22 Apr. 95	24
CAL9507	6 July 95	22 July 95	28
CAL9510	12 Oct. 95	26 Oct. 95	29
CAL9602	29 Jan. 96	10 Feb. 96	22
CAL9604	15 Apr. 96	30 Apr. 96	16
CAL9608	7 Aug. 96	25 Aug. 96	20
CAL9610	10 Oct. 96	1 Nov. 96	30
CAL9702	30 Jan. 97	2 Feb. 97	30
CAL9704	2 Apr. 97	17 Apr. 97	22
Total: 17 cruises			419 stations

Remote Sensing Reflectance vs. Chl

For a large dynamic range in surface pigments (chl a from 0.05 to 22.3 mg m^{-3}, [chl a + phaeo] from 0.06 to 27.2 mg m^{-3}) the CalCOFI data exhibit a relatively consistent pigment-reflectance relationship for the SeaWiFS bands (fig. 8). Some of the 304 measurements used for figure 8 were excluded from the final regressions if outside the 2 standard deviation range of the first robust least-deviation regression. The number of points outside the 2 standard deviation limits of the regression ranged from 7 at 665 nm to 19 at 510 nm. Compared to other bands, $R_{rs}(555)$ had the fewest excluded points, because noisier data at that wavelength resulted in a larger tolerance.

Chl Algorithms

When the $R_{rs}(443)/R_{rs}(555)$ and $R_{rs}(490)/R_{rs}(555)$ ratios were plotted against chl a, 11 of the more than 300 stations qualified as outliers because of various anomalies, and are not included in the analyzed data set. Some of the anomalies were explained by features like a shallow chl a maximum at about 10 m that influenced the R_{rs} but was not represented in the surface chl a sample, high soluble or sediment absorption at some coastal

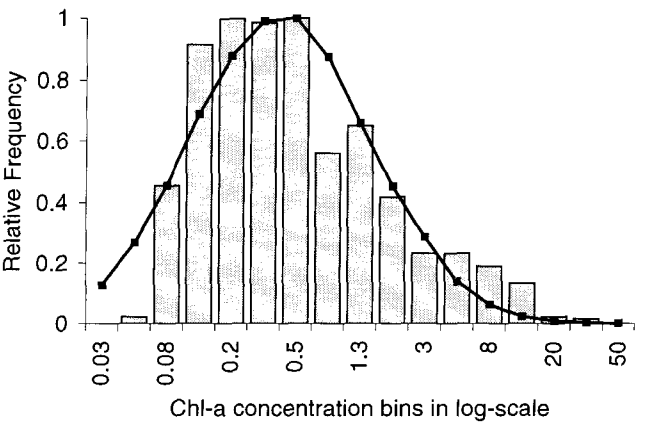

Figure 6. Relative frequency distribution (bars) of fluorometric chl a concentration for the upper 15 m in the CalCOFI data set. In total, 1,910 chl a measurements (all the CalCOFI cruises between 1993 and 1996) have been used, including those for stations with no bio-optical measurements. The mean is 1.07; the median is 0.31 mg m^{-3}. A theoretical lognormal distribution with the same mean and standard deviation is shown for comparison (continuous line).

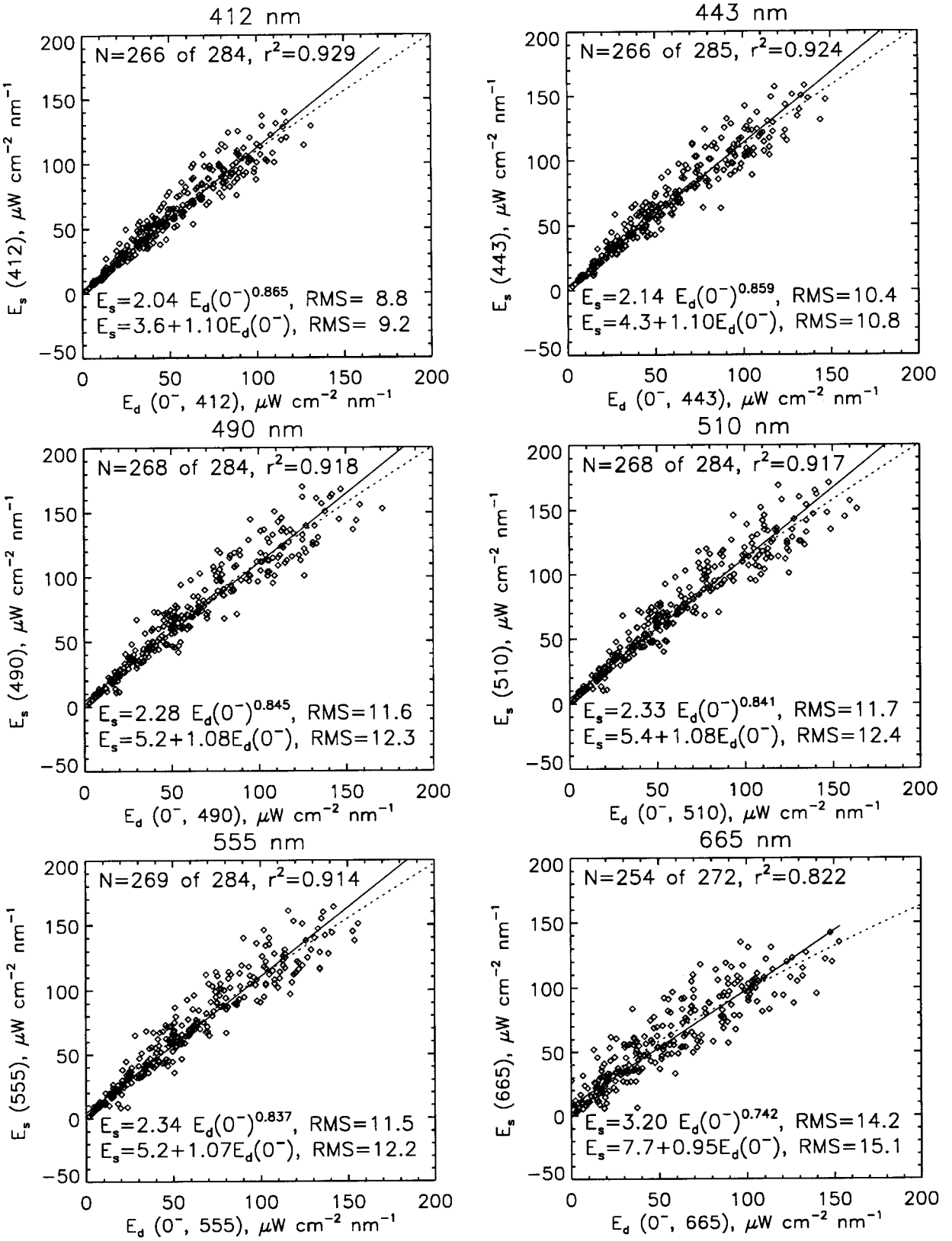

Figure 7. Surface irradiance $E_s(\lambda)$ as a function of the downwelling irradiance extrapolated to just below the surface $E_d(0^-,\lambda)$ from measurements of the underwater MER at the six SeaWiFS wavelengths. All values greater than the corresponding mean extraterrestrial irradiance $F_0(\lambda)$ (caused by wave focusing) were considered errors and were excluded. The remaining N_T points were fit to a linear regression, and all points deviating more than two standard deviations from the regression line (attributed to temporal/spatial offsets of cloud or ship shadow) were excluded. The remaining N points were fit with both reduced major axis linear regression and a power function. The respective sample size ("N of N_T"), coefficients, and root mean square errors are shown.

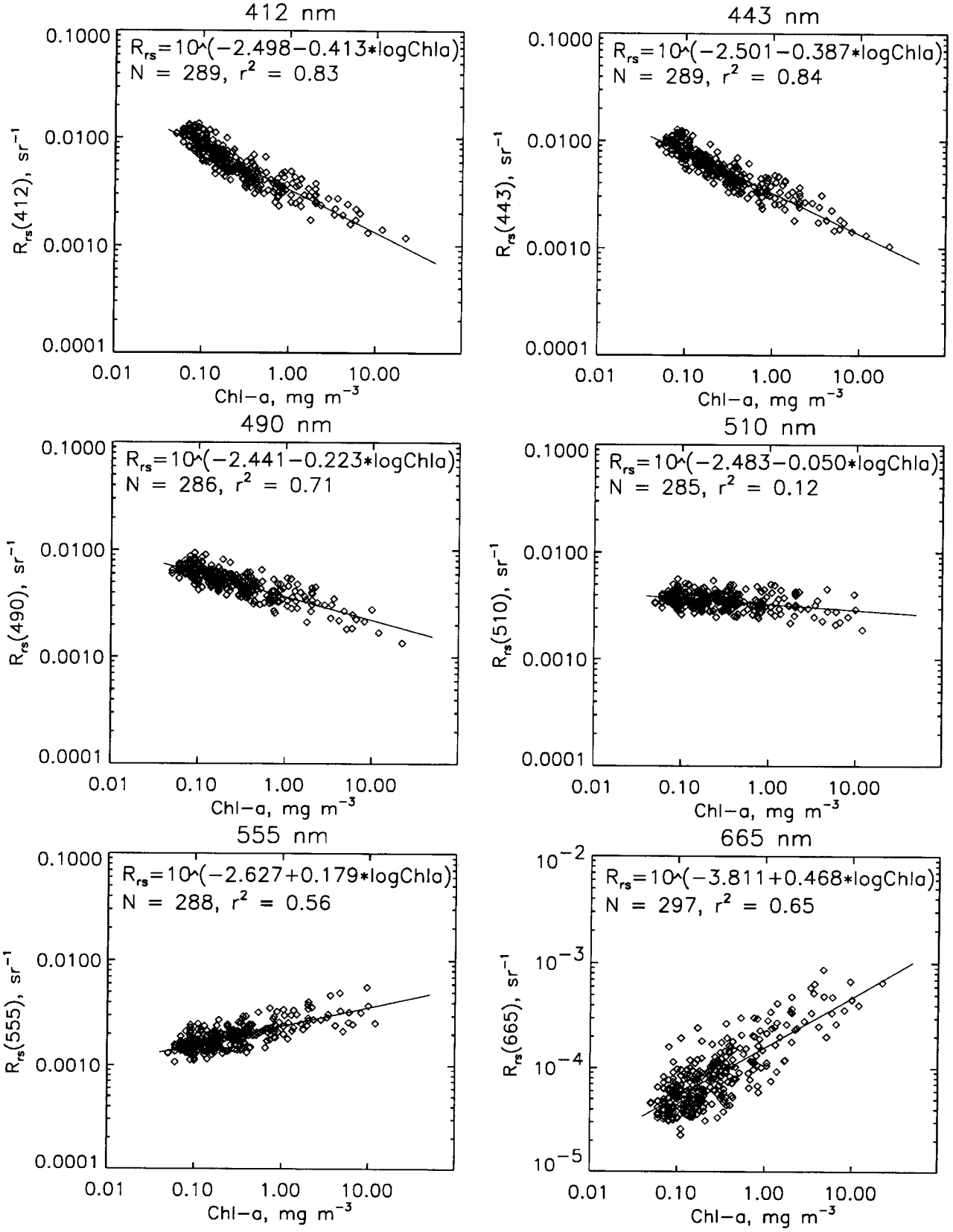

Figure 8. Remote sensing reflectance at the six SeaWiFS wavelengths as a function of chl a concentration. The points deviating more than 2 s.d. from an initial regression were excluded from the plots and the final statistical fit. Because the total data set consists of 304 observations, the number excluded can be determined on the basis of *N* reported for each wavelength.

stations, or high pigment packaging for some diatom blooms. Others had no obvious explanations. Of the 304 stations included in the CalCOFI data set, some surface extrapolated radiometric bands are still suspect, especially at 665 nm. Because of high absorption by water at 665 nm, the depth range that could be used for surface extrapolation was restricted to shallower depths that were more contaminated by ship shadow and other near-surface effects.

The consistency of the data set including all 304 data points is evident by the high linear correlation between log-transformed chl a concentration and reflectance ratios (fig. 9). In the high chl a range the relationship has a significant curvature, especially in the $R_{rs}(443)/R_{rs}(555)$ plot, which is not well described by the linear regression model. The relation between chl a and $R_{rs}(490)/R_{rs}(555)$ is closer to linear in the log-log space, has less variability, and in general has proven to be one of the most useful ratios in chl a prediction. This is attributed to three main causes: detrital and soluble absorption are lower at 490 nm compared to 443 nm, and pigment package effects are less at 490 nm because of weaker total absorption by the phytoplankton.

Linear models of both the log-log-transformed chl a or chl a + phaeo vs. $R_{rs}(490)/R_{rs}(555)$ (table 4, equations 3a, b) achieve r^2 of about 0.955 (fig. 10, upper panel). Although the linear fit in log-log space for the entire data set is practically unbiased (intercept of 0.0 and slope of 1.0), there is systematic underestimation at higher chl a. A quadratic fit was evaluated but did not bend toward the pure water value at low chl a (data not presented). A cubic polynomial fit has more parameters to force it to bend toward the pure water value at low chl a. But because of the absence of chl a concentrations less than 0.05 mg m^{-3}, the downward bend in the CalCOFI data was insignificant (fig. 9), and the least squares fit of a cubic polynomial (table 4, equations 4a, b) curved in the opposite direction.

In order to force the model into the correct direction at low chl a, we added another empirical coefficient to the cubic polynomial (table 4, equations 5a–d), following the Ocean Chlorophyll 2 (OC2) model (O'Reilly et al., in press). The resulting model ("CalCOFI Cubic A4"; fig. 10) improves the estimates at both high and low chl a ranges and reduces the overall RMS error. The sigmoid curvature of the OC2 model of O'Reilly et al. tuned to the global data set seemed to be too strong for the CalCOFI data set and resulted in higher RMS error, 0.129 of the OC2 model vs. 0.101 of the CalCOFI Cubic A4 model. The better fit to the CalCOFI data set of the Cubic A4 model is evident, especially in the middle chl a range of 0.2–3.0 mg m^{-3} (fig. 9, lower panel). Although the exact coefficients of the Cubic A4 model may undergo small changes as more data become available in the high and low chl a domains, models of the OC2 and CalCOFI Cubic A4 type are preferable to other empirical and semianalytical models that have been tested.

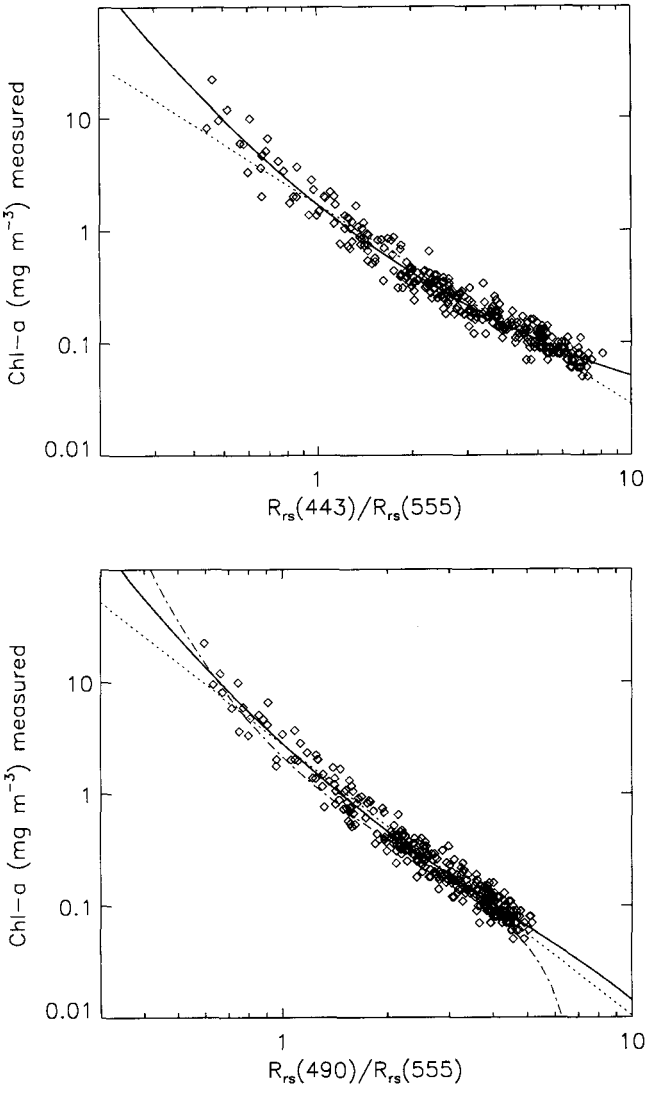

Figure 9. Near-surface chl a concentration as a function of $R_{rs}(443)/R_{rs}(555)$ and $R_{rs}(490)/R_{rs}(555)$ with reduced major axis linear regression (dotted straight line); CalCOFI Cubic A4 model (bold curved line, equations 5a and 5c, respectively, in table 4); and the OC2 model (dash-dot line) proposed by O'Reilly et al. (in press). The regression results are given in table 4.

Even with the coefficient of determination between the measured and predicted chl a above 0.95, there is still substantial variability around the regression line; this variability is even more accentuated in the linear scale than in the logarithmic scale. If part of the variability is due to accessory pigments, colored dissolved organic material (CDOM), or other spectrally dependent phenomena, then appropriate additional bands could explain some of the variability and reduce the RMS error of the prediction. To test this hypothesis, we evaluated multiple linear regressions between two log-transformed

TABLE 4
Evaluation of Algorithms for Estimating chl a and Pigment Concentrations (chl a + phaeo) from Remote Sensing Reflectance Ratios

Model	a intercept	b slope	r^2	RMS error	Equation number
CalCOFI 2-band linear model (*CalCOFI 2-Band*)					
chl a = 10.^{0.444 − 2.431 log[R_{rs}(490)/R_{rs}(555)]}	0.000	1.000	0.955	0.108	3a
chl a + phaeo = 10.^{0.557 − 2.440 log[R_{rs}(490)/R_{rs}(555)]}	0.000	1.000	0.956	0.107	3b
CalCOFI 2-band cubic model (*CalCOFI Cubic*)					
chl a = 10.^(0.450 − 2.860 R + 0.996 R^2 − 0.367 R^3) where R = log[R_{rs}(490)/R_{rs}(555)]	−0.012	0.980	0.960	0.101	4a
chl a + phaeo = 10.^(0.564 − 2.753 R + 0.571 R^2 − 0.002 R^3) where R = log[R_{rs}(490)/R_{rs}(555)]	−0.010	0.980	0.959	0.102	4b
CalCOFI Cubic A4					
chl a = 10.^(0.239 − 2.224 R + 0.888 R^2 − 0.053 R^3) − 0.02 where R = log[R_{rs}(443)/R_{rs}(555)]	−0.012	0.978	0.959	0.103	5a
chl a + phaeo = 10.^(0.357 − 2.185 R + 0.665 R^2 − 0.1018 R^3) − 0.02 where R = log[R_{rs}(443)/R_{rs}(555)]	−0.009	0.979	0.959	0.102	5b
chl a = 10.^(0.455 − 2.842 R + 1.000 R^2 − 0.080 R^3) − 0.02 where R = log[R_{rs}(490)/R_{rs}(555)]	−0.011	0.978	0.960	0.101	5c†
chl a + phaeo = 10.^(0.568 − 2.740 R + 0.571 R^2 − 0.2411 R^3) − 0.02 where R = log[R_{rs}(490)/R_{rs}(555)]	−0.009	0.978	0.959	0.102	5d†
CalCOFI 3-band model					
chl a = exp(1.025 − 1.622 ln[R_{rs}(490)/R_{rs}(555)] − 1.238* ln[R_{rs}(510)/R_{rs}(555)]	−0.013	0.978	0.956	0.106	6a
chl a + phaeo = exp(1.265 − 1.937 ln[R_{rs}(490)/R_{rs}(555)] − 0.737* ln[R_{rs}(510)/R_{rs}(555)]	−0.010	0.978	0.956	0.106	6b
CalCOFI 4-band model					
chl a = exp(0.753 − 2.583 ln[R_{rs}(443)/R_{rs}(555)] + 1.389* ln(R_{rs}(412)/R_{rs}(510)]	−0.013	0.977	0.956	0.106	7a
chl a + phaeo = exp(0.995 − 2.528 ln[R_{rs}(443)/R_{rs}(555)] + 1.285* ln[R_{rs}(412)/R_{rs}(510)]	−0.010	0.978	0.957	0.105	7b
OC2 (O'Reilly et al. 1998)	−0.085	0.976	0.955	0.129	
OC4 (O'Reilly et al. 1998)	−0.045	0.991	0.957	0.112	

†Preferred models for estimating chl a and chl a + phaeo for the CalCOFI data set.

R_{rs} ratios and chl a. We ran all possible combinations of the two R_{rs} ratio combinations, and selected the combinations with highest r^2 and lowest RMS error. The best combination using three bands is given by equations 6a, b; the best 4-band combination is given by equations 7a, b in table 4.

In essence, very little (if any) additional information was gained by including other band ratios besides $R_{rs}(490)/R_{rs}(555)$ to estimate chl a or [chl a + phaeo]. Although the 3- and 4-band combinations resulted in a slightly lower RMS error compared to the single linear $R_{rs}(490)/R_{rs}(555)$ ratio model, they were inferior to the quadratic and cubic fits of the $R_{rs}(490)/R_{rs}(555)$ ratio. Using more than one band ratio may be advantageous in cases of high variability caused by instrumental and environmental noise or for quality control. But it appears that the 3- and 4-band models tend to be specific to the particular data set and not robustly applicable to other data sets. As a result, the best combinations of bands changed when more data points were added to the CalCOFI data set.

For actual satellite applications, algorithms using more bands will be complicated by the need to know the on-orbit calibration time series of all the bands used. Clearly, simple 2-band algorithms will pose a simpler challenge for maintaining robust algorithms during a satellite's mission life. However, the sensitivity of multiband multiple regression models may be used for screening the data set for possible inconsistencies.

In conclusion, it appears that the residual noise is due predominantly to methodological errors and environmental variability and not to other optically significant components that should covary with band ratios other than $R_{rs}(490)/R_{rs}(555)$ (e.g., accessory pigments, CDOM). Bio-optical measurements at sea have significant variability due to illumination conditions, ship shadow, instrument tilt, and other methodological effects that cannot be completely eliminated and contribute to the residual RMS error.

With the coefficient of determination (r^2) greater than 0.96 between the log-transformed variables of a simple R_{rs} ratio model for chl a, it is unlikely that more advanced bio-optical models can produce a significant improvement. However, advanced models may extend the chl a range or provide additional variables besides chl a; e.g., CDOM, $a_{ph}(\lambda)$, coccoliths, backscattering coefficient, suspended sediments (Doerffer and Fischer 1994; Garver and Siegel 1997).

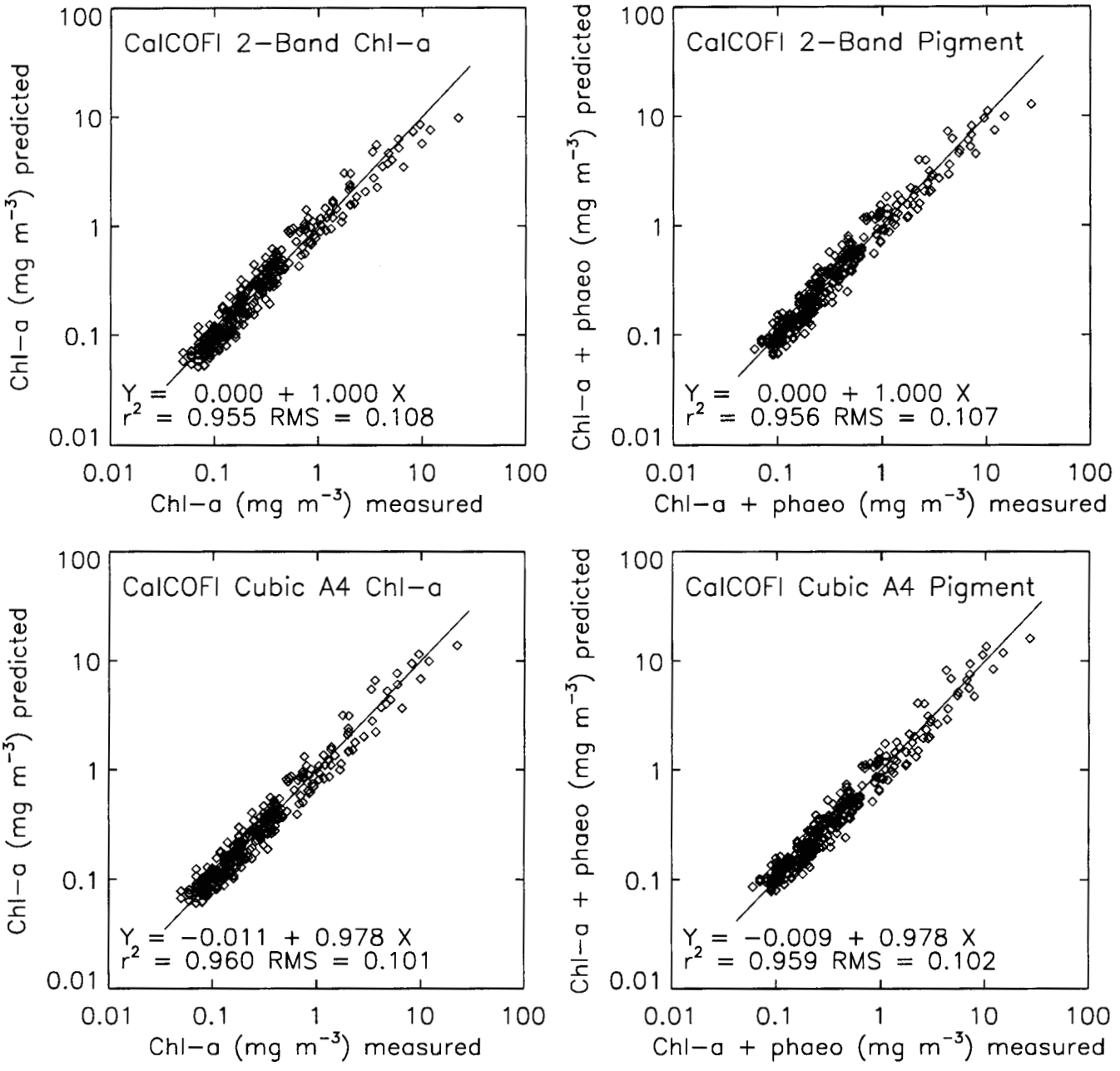

Figure 10. Results of the CalCOFI 2-band linear algorithm (top, equations 3a, b in table 4) and the CalCOFI Cubic A4 algorithm (bottom, equations 5a–d in table 4). Both algorithms use the ratio $R_{rs}(490)/R_{rs}(555)$. The one-to-one lines are shown.

$K_d(490)$ Algorithm

Since the work of Jerlov (1976), it has been assumed that the diffuse attenuation coefficient for downwelling irradiance $K_d(\lambda)$ at any wavelength can be expressed as a linear combination of K_d at a reference wavelength (e.g., 490 nm). At low K_d values this is a good approximation. Austin and Petzold (1984) have tabulated the slopes M (λ) from the equation

$$[K_d(\lambda) - K_w(\lambda)] = M(\lambda)\,[K_d(490) - K_w(490)]. \quad (8)$$

They used values of K_w that were very close to those of Smith and Baker (1981) or Morel and Prieur (1977).

New values of pure water absorption have recently been determined with an integrating cavity absorption meter (Pope and Fry 1997), and there are some concerns within the ocean optics community that the values of K_w or a_w used in previous literature may be too high, especially between 400 and 500 nm. For the analysis presented here, we used values of K_w from Morel (1988) for data between 400 and 700 nm and from Smith

and Baker (1981) for wavelengths below 400 nm. In figure 11 a comparison between the CalCOFI data set and the results of Austin and Petzold (1984) for the coefficient M indicate good agreement between the CalCOFI data set and theirs, when similar methods were used.

The relation between chl a and $K_d(\lambda) - K_w(\lambda)$ has been studied by many investigators (e.g., Baker and Smith 1982; Morel 1988; Mitchell 1992). Figure 12 indicates that this relation is not well described by a linear fit in the log-log space for SeaWiFS wavelengths 412, 443, and 455 nm. Baker and Smith (1982) fit their data with a nonlinear function in log space, whereas Morel (1988) used a power law model (equivalent to linear in the log-log space). Some of the curvature observed between 400 and 460 nm at low chl a, also observable in the Baker and Smith fit, could be caused by subtraction of K_w that is larger than the true value of K_w. The K vs. chl a and $K(\lambda)$ vs. $K_d(490)$ relationships should be reevaluated with modern estimates of the absorption and K values for pure water (Pope and Fry 1997).

A simple band-ratio approach was used to estimate $K_d(490)$ from the normalized water-leaving radiance data following the original approach for CZCS (Austin and Petzold 1981). In spite of the high variability at low $K_d(490)$ (fig. 13), the equation that we obtained by using the "robust" least absolute deviation linear regression

$$K_d(490) = 0.022 + 10\text{^}[-0.964 - 1.301 * \log (L_{WN}(443)/L_{WN}(555))] \quad (9)$$

is in excellent agreement with the recent estimate of Mueller and Trees (1996). Mueller and Trees concluded that the data set they had compiled (including some CalCOFI data) led to a regression that was significantly different, in a statistical sense, from the regression used for CZCS. This may in part be attributed to the difference between the 550 nm band in CZCS and the 555 nm band used in this data set and in that of Mueller and Trees. The good agreement between Mueller and Trees (1996) and the results presented here indicates that the simple method we used to estimate surface layer K is consistent with the integral least-squares method of Mueller (1991).

The ratio of $L_{WN}(490)/L_{WN}(555)$ instead of $L_{WN}(443)/L_{WN}(555)$ gives a slightly higher r^2 and lower RMS error (fig. 13, lower panel) and proved more reliable for ocean color applications in cases of very high 443 nm absorption (e.g., in red tide or other blooms or when CDOM in coastal waters is very large). The equation using the $L_{wn}(490)/L_{wn}(555)$ ratio is

$$K_d(490) = 0.022 + 10\text{^}[-0.813 - 1.636 * \log (L_{WN}(490)/L_{WN}(555))]. \quad (10)$$

The improvement using the $L_{wn}(490)/L_{wn}(555)$ ratio compared to $L_{wn}(443)/L_{wn}(555)$ ratio is also found for

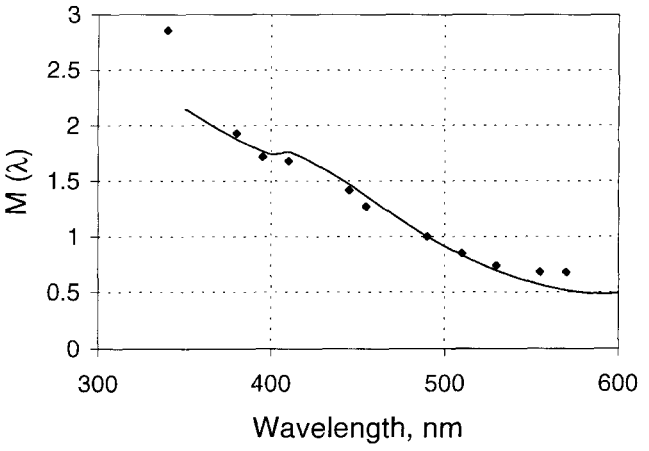

Figure 11. Slope $M(\lambda)$ for equation 8 from Austin and Petzold 1986 (continuous line) compared to CalCOFI data (filled symbols). Only $K_d(490)$ less than 0.1 m^{-1} were used to estimate $M(\lambda)$.

empirical chl a algorithms (see previous section Chl Algorithms). NASA's global processing for chl a exploits the improved empirical regressions using $L_{wn}(490)/L_{wn}(555)$ but uses $L_{wn}(443)/L_{wn}(555)$ for $K_d(490)$. We believe that $L_{wn}(490)/L_{wn}(555)$ provides a sufficiently better empirical fit for $K_d(490)$ and that NASA should consider using it in global processing.

CONCLUSIONS

A set of more than 300 concurrent measurements of remote sensing reflectance, chl a, and diffuse attenuation coefficients has been analyzed. The CalCOFI data set comprises more than 30% of the total "global" data set that was assembled by the SeaWiFS Project for this effort (O'Reilly et al., in press). In general, the CalCOFI data set was consistent with the other global data and covered all but the lowest pigment range (chl a < 0.05 mg m^{-3}).

Evaluation of empirical algorithms and semianalytical models shows that simple empirical algorithms perform better than semianalytical models at this time for SeaWiFS standard products including chl a, chl a + phaeo, and $K_d(490)$. Relatively little, if any, improvement in estimation is attained by using more complex sets of multiband ratios for this type of empirical algorithm. Given the added complexity of accurate knowledge of the on-orbit calibration if multiple spectral bands are used, it seems advisable to use the $R_{rs}(490)/R_{rs}(555)$ ratio as a basis for global processing algorithms for chl a and chl a + phaeo. It may be advisable, as well, to consider this band ratio for the $K_d(490)$ algorithm, given the improvement that was found with the CalCOFI data set using $L_{WN}(490)/L_{WN}(555)$ compared to $L_{WN}(443)/L_{WN}(555)$. It is also important to recognize that previous $K_d(490)$ algorithms depend partly on assumptions about the value of K for pure water. Those assump-

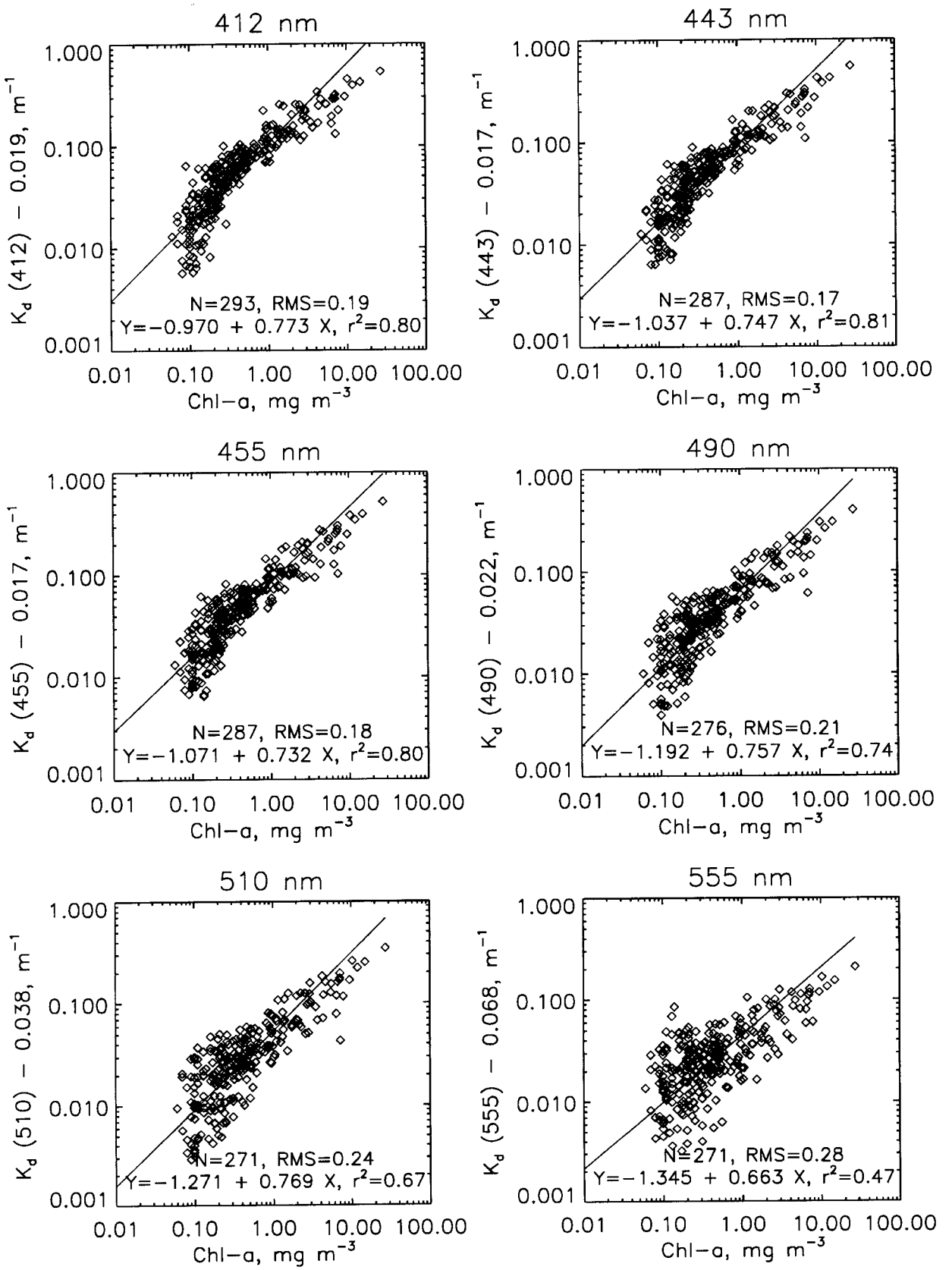

Figure 12. $K_d(\lambda) - K_w(\lambda)$ as a function of chl a concentration. The $K_w(\lambda)$ values are from Morel 1988. The lines are reduced major axis linear regressions in the log-log space.

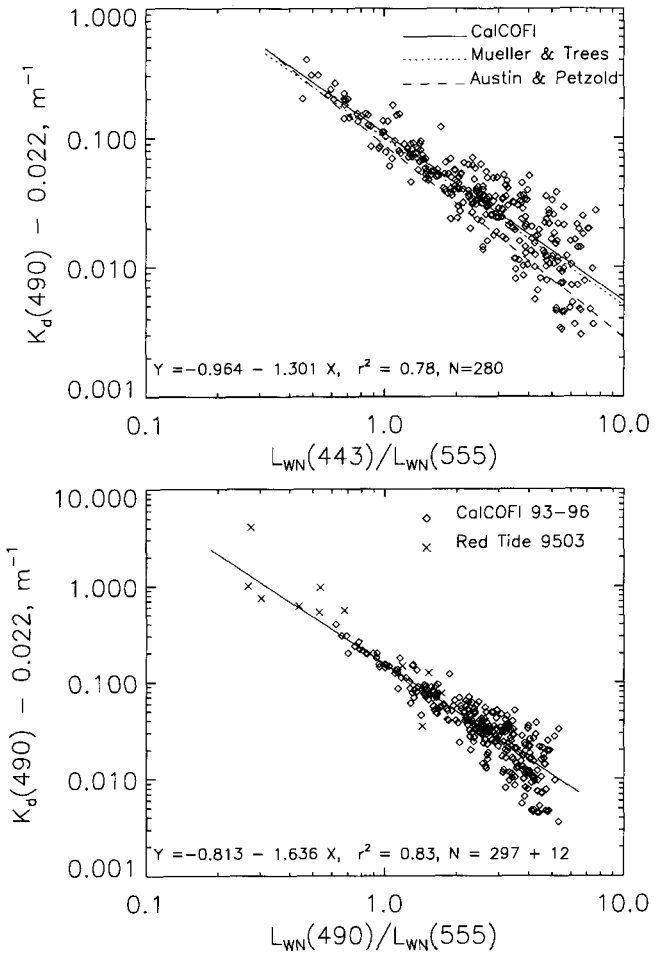

Figure 13. Upper panel, $K_d(490)$ as a function of the ratio of normalized water-leaving radiances $L_{wn}(443)/L_{wn}(555)$. A comparison of the CalCOFI estimate (equation 9) with the results of Mueller and Trees (1996) and Austin and Petzold (1981). Lower panel, $K_d(490)$ estimated from $L_{WN}(490)/L_{WN}(555)$ including data from a red tide cruise RED9503. The root mean square error and r^2 were calculated for the log-transformed data.

tions may now need to be revised, since recent laboratory measurements imply that the K for pure water in the region of relevance for SeaWiFS bio-optical algorithms may be smaller than previously reported.

ACKNOWLEDGMENTS

This work was supported by a grant from the NASA HQ Ocean Biogeochemistry Program and a cooperative agreement from NASA GSFC (NAGW-3665, NCC-5-48). We gratefully acknowledge BSI, Inc., CHORS, and ICESS for their efforts in characterizing and calibrating our radiometer; E. Brody and V. Fournier-Sicre for participating in some of the cruises, and for helping with the early development of the calibration time series procedures and processing schemes; the director's office of SIO and the Vettelson Foundation for providing matching funds for the NASA grant for several days of ship time to contribute to CalCOFI for part of the wire time; David Siegel for making the BBOP software available; the CalCOFI Committee for encouraging our participation in the CalCOFI cruises and providing very generous wire time to accomplish our work; the CalCOFI technicians for extraordinary analytical and data-reduction effort, and for their provision of the CalCOFI data sets; the SIO Marine Facility and resident technicians for assistance in configuring winches and laboratory vans for the cruises; and the captains and crews of the R/V *New Horizon* and R/V *David Starr Jordan* for their expert execution of the CalCOFI cruises.

LITERATURE CITED

Austin, R. W. 1974. Inherent spectral radiance signatures of the ocean surface. *In* Ocean color analysis, S. W. Duntley, R. W. Austin, W. H. Wilson, C. F. Edgerton, and S. E. Moran, eds. Univ. Calif. San Diego, SIO ref. 74-10, pp. 1–20.

Austin, R. W., and T. J. Petzold. 1981. The determination of the diffuse attenuation coefficient of sea water using the coastal zone color scanner. *In* Oceanography from space, J. F. R. Gower, ed. Plenum Publishing, pp. 239–256.

———. 1984. Spectral dependence of the diffuse attenuation coefficient of light in ocean waters. *In* Ocean optics VII, M. Blizard, ed. Bellingham, Wash.: SPIE, pp. 168–178.

Baker, K. S., and R. C. Smith. 1982. Bio-optical classification and model of natural waters, 2. Limnol. Oceanogr. 27:500–509.

Bricaud, A., M. Babin, A. Morel, and H. Claustre. 1995. Variability in the chlorophyll-specific absorption coefficients of natural phytoplankton: analysis and parameterization. J. Geophys. Res. 100(C7):13,321–13,332.

Campbell, J. W., and J. E. O'Reilly. 1988. Role of satellites in estimating primary productivity on the northwest Atlantic continental shelf. Cont. Shelf Res. 80:179–204.

Doerffer, R., and J. Fischer. 1994. Concentrations of chlorophyll, suspended matter, and gelbstoff in case II waters derived from satellite coastal zone color scanner data with inverse modeling methods. J. Geophys. Res. 99(C4):7457–7466.

Garver, S. A., and D. A. Siegel. 1997. Inherent optical property inversion of ocean color spectra and its biogeochemical interpretation 1. Time series from the Sargasso Sea. J. Geophys. Res. 102(C8):18,607–18,625.

Goericke, R., and D. J. Repeta. 1993. Chlorophylls a and b and divinyl chlorophylls a and b in the open subtropical North Atlantic Ocean. Mar. Ecol. Prog. Ser. 101:307–313.

Gordon, H. R., and K. Ding. 1992. Self-shading of in-water optical instruments. Limnol Oceanogr. 37:491–500.

Gordon, H. R., D. K. Clark, J. W. Brown, O. B. Brown, R. H. Evans, and W. W. Broenkow. 1983. Phytoplankton pigment concentrations in the Middle Atlantic Bight: comparison of ship determinations and CZCS estimates. Appl. Optics 22:20–36.

Holm-Hansen, O., C. J. Lorenzen, R. W. Holmes, and J. D. H. Strickland. 1965. Fluorometric determination of chlorophyll. J. Cons. Explor. Int. Mer. 30:3–15.

Jerlov, N. G. 1976. Marine optics. Elsevier Scientific Publ., 231 pp.

Kahru, M., and B. G. Mitchell. In press. Spectral reflectance and absorption of a massive red tide off southern California. J. Geophys. Res.

Laws, E. A., and J. W. Archie. 1981. Appropriate use of regression analysis in marine biology. Mar. Biol. 65:269–279.

Mitchell, B. G. 1992. Predictive bio-optical relationships for polar oceans and marginal ice zones. J. Mar. Syst. 3:91–105.

Mitchell, B. G., and D. A. Kiefer. 1988. Variability in pigment specific particulate fluorescence and absorption spectra in the northeastern Pacific Ocean. Deep-Sea Res. 35:665–689.

Morel, A. 1988. Optical modeling of the upper ocean in relation to its biogenous matter content (case I waters). J. Geophys. Res. 93(C9): 10,749–10,768.

Morel, A., and L. Prieur. 1977. Analysis of variations in ocean color. Limnol. Oceanogr. 22:709–722.

Mueller, J. L. 1991. Integral method for irradiance profile analysis. CHORS Tech. Memo. 007–91, San Diego State Univ., San Diego, Calif. 10 pp.

———. 1995. Comparison of irradiance immersion coefficients for several marine environmental radiometers (MERs). *In* NASA Tech. Memo. 104566, S. B. Hooker, E. R. Firestone, and J. G. Acker, eds. NASA Goddard Space Flight Center, Greenbelt, Md., 27:3–18.

Mueller, J. L., and R. W. Austin. 1995. Ocean optics protocols for Sea WiFS validation, revision 1. *In* NASA Tech. Memo. 104566, S. B. Hooker, E. R. Firestone, and J. G. Acker, eds. NASA Goddard Space Flight Center, Greenbelt, Md., 25:1–66.

Mueller, J. L., and C. C. Trees. 1996. Revised SeaWiFS pre-launch algorithm for the diffuse attenuation coefficient $K_d(490)$. CHORS Tech. Memo. 006-96, San Diego State Univ., San Diego, Calif., 9 pp.

Mueller, J. L., B. C. Johnson, C. L. Cromer, J. W. Cooper, J. T. McLean, S. B. Hooker and T. L. Westphal. 1994. The second SeaWiFS intercalibration round-robin experiment, SIRREX-2, June 1993. *In* NASA Tech. Memo. 104566, S. B. Hooker, E. R. Firestone, and J. G. Acker, eds. NASA Goddard Space Flight Center, Greenbelt, Md., 16:1–1210.

O'Reilly, J. E., S. Maritorena, B. G. Mitchell, D. A. Siegel, K. L. Carder, S. A. Garver, M. Kahru, and C. R. McClain. In press. Ocean color chlorophyll algorithms for SeaWiFS. J. Geophys. Res.

Pope, R. M., and E. S. Fry. 1997. Absorption spectrum (380–700 nm) of pure water: II. Integrating cavity measurements. Appl. Optics 36:8710–8723.

Press, W. H., S. A. Tuekolsky, W. T. Wettering, and B. P. Flannery. 1990. Numerical recipes in C: the art of scientific computing. Cambridge Univ. Press, 994 pp.

Ricker, W. E. 1973. Linear regressions in fisheries research. J. Fish. Res. Board Can. 30:409–434.

Siegel, D. A., M. C. O'Brien, J. C. Sorensen, D. A. Konnoff, and E. Fields. 1995. BBOP data processing and sampling procedures. US JGOFS planning and coordination. U.S. JGOFS Planning and Coordination Office, Woods Hole Oceanographic Inst., Woods Hole, Mass., 19, 77 pp.

Smith, R. C., and K. S. Baker. 1978a. Optical classification of natural waters. Limnol. Oceanogr. 23:260–267.

———. 1978b. The bio-optical state of ocean waters and remote sensing. Limnol. Oceanogr. 23:247–259.

———. 1981. Optical properties of the clearest natural waters (200–800 nm). Appl. Optics 20:177–184.

Sosik, H. M., and B. G. Mitchell. 1995. Light absorption by phytoplankton, photosynthetic pigments, and detritus in the California Current System. Deep-Sea Res. 42:1717–1748.

Venrick, E. L., and T. L. Hayward. 1984. Determining chlorophyll on the 1984 CalCOFI surveys. Calif. Coop. Oceanic Fish. Invest. Rep. 25:74–79.

GLOSSARY

Abbreviations

BBOP	Bermuda Bio-Optics Project
BSI	Biospherical Instruments, Inc.
CDOM	Colored dissolved organic material
CHORS	Center for Hydro-Optics and Remote Sensing (San Diego State University)
CZCS	Coastal Zone Color Scanner
HPLC	High-performance liquid chromatography
ICESS	Institute for Computational Earth System Science (University of California, Santa Barbara)
IEH	File format of the CalCOFI data archive
IRIX	A computer operating system
LCD	Least common denominator (data file format)
MER	Multispectral Environmental Radiometer
Perl	A programming language
RMS	Root mean square (error)
SeaBASS	SeaWiFS Bio-optical Archive and Storage System
SIRREX	SeaWiFS Intercalibration Round-Robin Experiment

Symbols

λ	Wavelength, nm
$a_{ph}(\lambda)$	Phytoplankton pigment spectral absorption coefficient
$a_w(\lambda)$	The absorption coefficient for pure water
$E_d(\lambda)$	Downwelling spectral irradiance
$E_d(0^-,\lambda)$	Downwelling spectral irradiance just below the sea surface
$E_s(\lambda)$	Surface irradiance
$F_0(\lambda)$	Mean extraterrestrial spectral irradiance
$K_d(\lambda)$	Diffuse attenuation coefficient of seawater for downwelling irradiance
$K_d(490)$	Diffuse attenuation coefficient of seawater for downwelling irradiance measured at 490 nm
$K_w(\lambda)$	Diffuse attenuation coefficient of pure seawater
$L_u(\lambda)$	Upwelling spectral radiance
$L_{WN}(\lambda)$	Normalized water-leaving radiance
$M(\lambda)$	The slope coefficient between different spectral K values
phaeo	Phaeopigment concentration
$R_{rs}(\lambda)$	Remote sensing reflectance
$R_{rs}(0^-,\lambda)$	Remote sensing reflectance just below the sea surface
$R_{rs}(0^+,\lambda)$	Remote sensing reflectance just above the sea surface